Earth, Planets and Space

FULL PAPER Open Access

How geomagnetic storms affect the loss of Starlink satellites in February 2022?

Nizam Ahmad[1*], La Ode Muhammad Musafar Kilowasid[2], Hanif Fakhrurroja[3*], Neflia[1], Abdul Rachman[4], Asnawi Husin[1] and Haries Fathoni[1]

Abstract

On February 8, 2022, approximately 40 of the 49 Starlink satellites were reported to have lost altitude, leading to atmospheric re-entry. SpaceX reported that the orbital decay on Starlink satellites was considered to be linked to a geomagnetic storm that was initiated on February 3, 2022. We attempted to analyze the cause of orbital decay by sampling all Starlink satellites registered in the SpaceTrack database and then tracing some space weather parameters and species density variations in the thermospheric layer. We employed the solar wind and IMF *Bz* to see their impact on geomagnetic activity. Moreover, we also analyzed the electric field *Ey*, *Dst*, *AE*, and *Ap* indices in addition to the solar EUV flux to see their impact on the Starlink satellite environment. We discovered three geomagnetic substorms during the analysis period: two successive substorms on February 4 and 5, and one additional substorm on February 10. We inferred that magnetic substroms significantly affected species densities, mainly O, O_2, and N_2, around some Starlink satellites, leading to an increase in atmospheric drag. There was a time delay between the substorms and orbital decay on Starlink satellites. However, some Starlink satellites were not affected by geomagnetic substorms due to insignificant changes in their environment. The reason for this is that, despite having lower altitudes, all decaying Starlinks were located in the midnight-dawn sector, in which the drift of ionospheric currents was predominantly driven by westward electrojets. On the other hand, all non-decaying Starlink satellites that had higher altitudes resided in the dusk–midnight sector of magnetic local time, where the impact of substorms insignificantly affected their altitudes.

Keywords Starlink satellites, Geomagnetic storms, Orbital decay

*Correspondence:
Nizam Ahmad
ncjam_a@yahoo.com; nizam.ahmad@brin.go.id
Hanif Fakhrurroja
haniff@telkomuniversity.ac.id
Full list of author information is available at the end of the article

Graphical Abstract

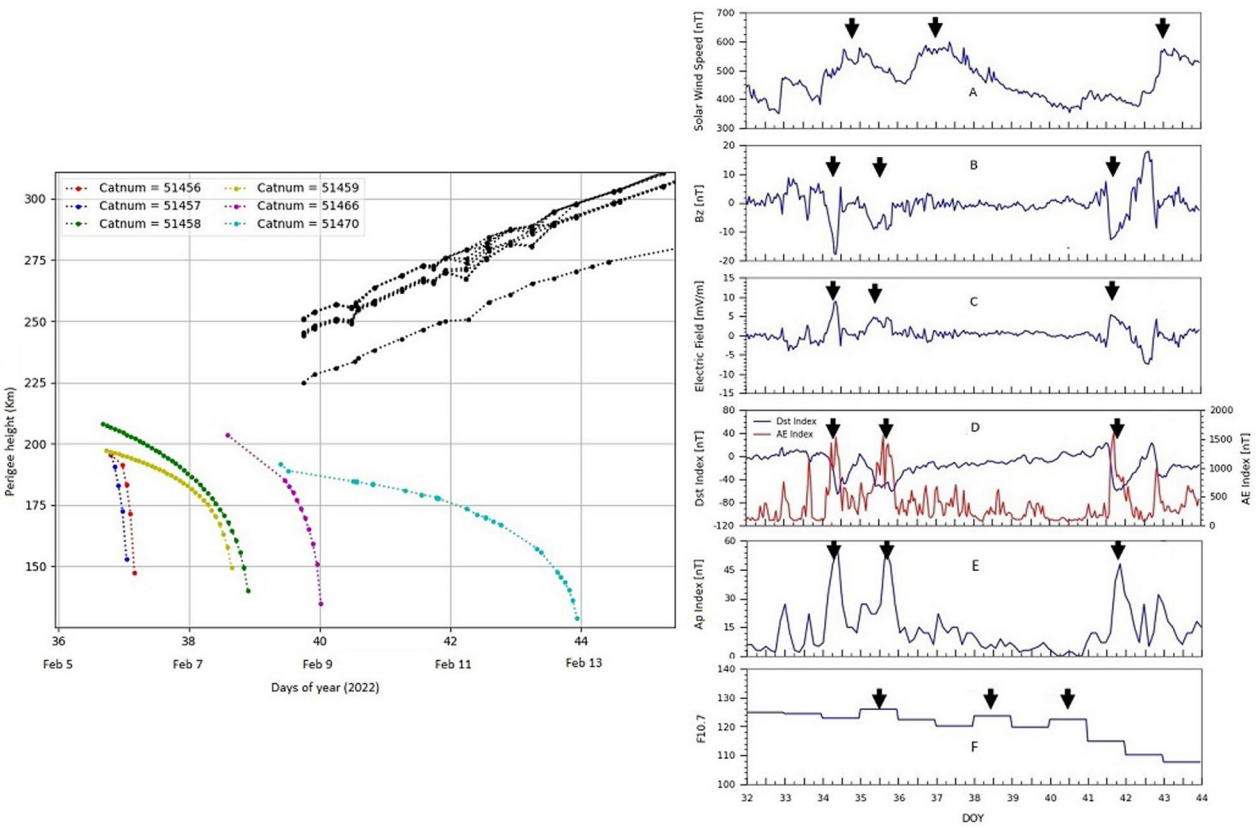

1 Introduction

Perturbations on satellites in both low earth orbit (LEO) and geosynchronous earth orbit (GEO), depending on the type of perturbation, are in most cases related to the dynamics of space weather or the space environment around the satellite, which is primarily triggered by various solar events such as flares, coronal mass ejections (CMEs), and corotating interaction regions (CIRs), which then affect the earth's magnetic field (Patil et al. 2008). Changes in the earth's magnetic field then influence particle properties like density, flux, and ambient temperature of the plasma scattered around the satellite (Shea and Smart 1998).

The abrupt change in ambient plasma due to particle penetration associated with changes in the earth's magnetic field tends to cause disturbances not only in satellite operation but also in its orbit (Tribble 2003). The effects of geomagnetic storms on satellite operations can be seen from October to November 2003, in which approximately 25 satellites at different altitudes were disturbed due to geomagnetic storms, which occurred primarily in the inner part of the radiation belt (Webb and Allen 2004). In spite of affecting satellite operation, geomagnetic storms or substorms can also influence changes in atmospheric density, which tend to cause the density to increase (Ren et al. 2022). The increase in species density leads to a decrease in satellite altitude. The drop in altitude can cause the satellite to re-enter the atmosphere in extreme conditions. Several studies have found that the decay or re-entry of some space objects is linked to geomagnetic storms or sub-storms. (Nwankwo et al. 2021; Li and Lei 2021).

Perturbation on satellites caused by sudden changes in atmospheric densities has been discovered, for instance, during the "Bastille Day" geomagnetic storm (July 14–15, 2000), in which the Astro-D satellite lost its altitude (Cannon 2013). The effects of geomagnetic storms affecting satellites altitudes were also found on other LEO satellites, such as those experienced by CHAMP (Challenge Mini-satellite Payload) and GRACE (Gravity Recovery and Climate Experiment) in 2005 (Krauss et al. 2018; Oliveira and Zesta 2019). They found that the mild

storms, rated as G2 on national oceanic and atmospheric administration (NOAA) geomagnetic storm scales, led to orbital decay on the CHAMP satellite, whereas GRACE altitude loss was attributed to the intense storms. Interestingly, geomagnetic storms such as the above event, but with a lower scale, also occurred on February 1–12, 2022, when numerous parameters showed an increase in magnetic activity and solar radiation flux and were considered to be related to the cause of orbital decay on several Starlink satellites.

This paper attempts to address an important question: "How did geomagnetic substorms, rather than just geomagnetic storms, contribute to the loss and re-entry of satellites such as Starlink?". The question was addressed through an investigation of the potential impact of magnetic fluctuations on satellite operations at the beginning of February 2022 by analyzing magnetic parameters, their impact on the thermospheric layer, and symptoms of satellite operational disturbances from February 1–12. We used the Starlink satellites as a case study because they have been reported by Space (2022) to suffer decay due to geomagnetic storms (https://www.space.com/spacex-starlink-satellites-lost-geomagnetic-storm). The cause of their orbital decays is still uncertain and requires further investigation.

Several studies have tried to answer the causes of decay in Starlink satellites, and most of them show an increase in neutral density due to geomagnetic storms. The study conducted by Fang et al. (2022) showed a density enhancement of around 50–125% at altitudes between 200 and 400 km. Model simulation driven by solar wind showed that on February 3 and 4, geomagnetic storms induced atmospheric density disturbances around 20% and 20–30%, respectively, at 210 km altitude (Dang et al. 2022). A study conducted by Berger et al. (2023) attempted to model the orbital altitude and in-track position of a Starlink-like satellite in a low-drag configuration at 200 km during minor (G1) and extreme (G5) geomagnetic storms and has employed NRLMSIS, JB08, and HASDM empirical models in their study. During the launch period for the Starlink satellite on February 3, there was an increase in thermospheric density of at least 20–30% at an altitude of 210 km compared to the period 9 days before launch. Furthermore, investigations carried out by Lin et al. (2022) using the Multiscale Atmosphere-Geospace Environment (MAGE) model showed that up to 150% density enhancement occurred during consecutive geomagnetic storms on 3–4 February, 2022. The recent study conducted by Kakoti et al. (2023) showed that there was a connection between geomagnetic storms of G1 class impacting the dayside ionospheric-thermospheric changes in the period 3–4 February 2022 that caused the loss of Starlink satellites. Moreover, Laskar et al. (2023) used the Globalscale Observations of Limb and Disk (GOLD) temperature observations to tune the MSIS model and showed that the neutral density increases in the thermosphere during the storm ranged from 15% at 150 km to about 80% at 500 km altitudes, which agrees with satellite observations (Billett et al. 2024). They also reported that the density difference at 210 km is about 25% and can range from 15 to 45%, depending on reference day.

Space X has reported that up to 40 Starlink satellites will or have already re-entered the earth's atmosphere at the time this report was released (February 8, 2022). However, we found that not all Starlink satellites experienced decay. We found a difference in position distribution between decayed Starlink satellites and non-decayed Starlink satellites in terms of their magnetic local times, as we will show in the next section. Thus, the goal of this paper is to further investigate the causes of orbital decay on some Starlink satellites by employing some key parameters.

1.1 Data and method

The data used in this study are classified into two categories: data involving multiple space weather parameters and satellite orbital decay data. Space weather covers data from solar wind speed (V_{SW}), interplanetary magnetic field (IMF *Bz*), electric field (*Ey*), geomagnetic activities represented by disturbance storm time (*Dst*), and auroral electrojet (*AE*) indices, in addition to the daily average of the geomagnetic activity index (*Ap*). We also employed the solar radiation extreme ultraviolet (EUV) index (*F*10.7) as a proxy for solar activity.

The solar wind is simply stated as the medium comprising tenuous magnetized plasma consisting of ions and electrons that flow from the sun. Its velocity ranges from 400 km/s (slow speed) to 750 km/s (fast speed), and its variability can affect the Earth's magnetosphere (Schwenn 2006). The interplanetary magnetic field (IMF) is a magnetic field embedded in the solar wind that can rotate it at some distance above the photosphere of the sun (Suess and Tsurutani 2003). The impact of solar wind through the transfer of energy and momentum on the Earth's magnetosphere can be measured from the *Bz* component of the IMF (Reiss et al. 2021). The interplanetary electric field (*Ey*) plays an important role in generating geomagnetic storms, and it is a product of solar wind velocity and southward IMF *Bz* (Nikolaeva et al. 2011). The *Dst* index is a measure of geomagnetic disturbance in the ring current. The *Dst* index drops significantly during geomagnetic storms (Fennell et al. 2001). The *AE* index is a quantitative measure of ionospheric currents in auroral regions (Burton et al. 1975). The solar EUV flux (*F*10.7) is a measure of radio emission from the sun at 10.7 cm

wavelength, and it can be a good indicator of solar activity. It is measured in solar flux units (sfu; 1 sfu = 10^{-22} W/m^2H_z) (Tapping 2013).

In this study, we first noted various solar occurrences that influence the solar wind's velocity (*Vsw*) and elevate radiation in the upper atmosphere, such as flares and CMEs. We concentrated on the rapid solar wind speed ($Vs > 500$ km/s) and solar EUV flux level ($F10.7 > 120$ sfu) in the current study. Since the IMF *Bz* variation is linked to the solar wind's *Ey* component, its effects on geomagnetic storms are manifested by an increase in the *AE* index and a decrease in the *Dst* index. The impact of magnetic storms on the thermospheric layer is identified through total electron content (TEC) variation. Most of the data used in the present study can be obtained from NASA's Goddard Space Flight Center (NASA GSFC) OMNIweb data documentation at https://omniweb.gsfc.nasa.gov.

In parallel, we analyzed the effects of solar radiation increasing in the atmosphere through rapid changes in concentration on some elements such as O, O_2, and N_2 using the NRLMSISE-00 (Naval Research Laboratory Mass Spectrometer and Incoherent Scatter Radar) model. In order to examine whether the changes in concentration in the parameters mentioned above affect all Starlink satellites, we track the converted satellite positions in satellite local time. We then employed this location to look for an increase in atmospheric drag, leading to altitude loss, in each case of the Starlink satellites taken as a case study.

In the present study, we used Starlink satellite data that had been reported to experience orbital decay a few days after their launch, linked to geomagnetic storms. We attempted to use an approach in which the variations in magnetic activity and solar flux radiation affecting the decay of the Starlink altitudes occurred sequentially throughout the analysis period. The schematic diagram in Fig. 1 briefly describes the method used in this paper.

Figure 1 shows how one data point is related to other data points in examining how geomagnetic storms affect the orbital decay of Starlink satellites. In the first step, reports of Starlink altitude loss became the point of interest in this investigation. In this case, data such as the time of the altitude loss, the satellite's position, and its estimated cause are used to statistically study the variation of all the parameters above within the period of February 1 to February 12, 2022. According to the SpaceX report, 49 Starlink satellites were launched on February 3, 2022, at 1:13 p.m. (local time) from a perigee altitude of approximately 210 km. On February 8, 2022, 40 of the 49 satellites announced had decayed, which is thought to be due to the impact of a magnetic storm that occurred one day after the satellite was launched on February 4, 2022, as reported by SpaceX(2022) at (https://www.spacex.com/updates/). However, in this study, we consider all Starlink satellites that have been registered with SpaceTrack, of which six have been reported as having lost altitude (decayed), while the other eleven are still in operation.

The next step was looking into the variation of the solar wind using the report of orbital decay on

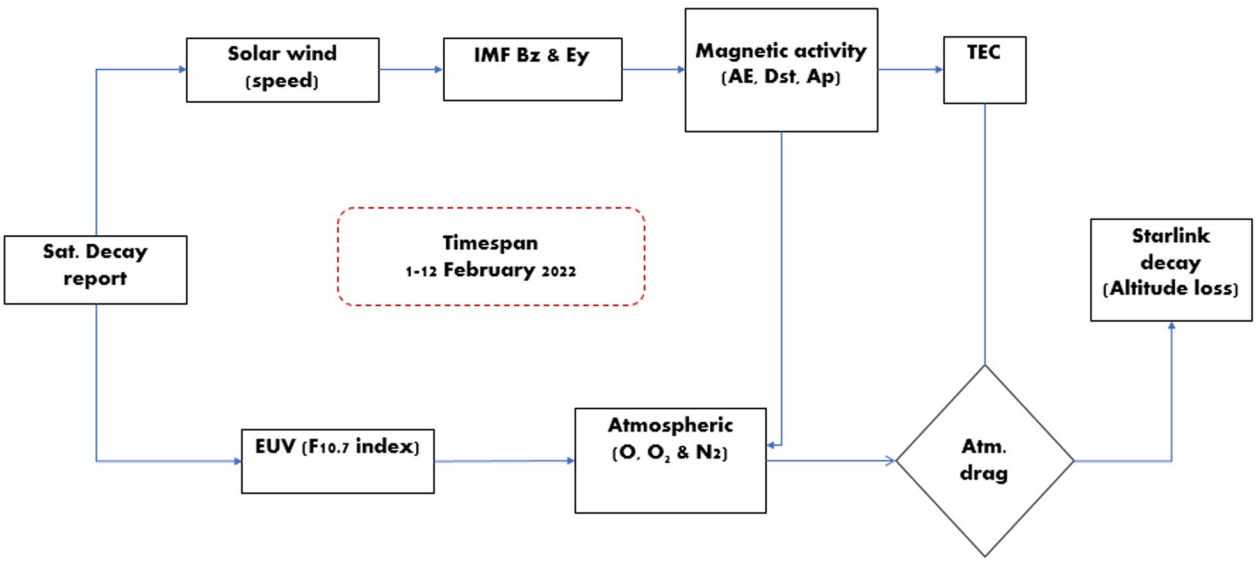

Fig. 1 Schematic diagram to estimate the potential cause of the Starlink satellite's loss. The arrows in this diagram show how one data point is linked with other data points in examining how geomagnetic storms affect the decay of Starlink satellites (Community Coordinated Modelling Center 2022)

Starlink satellites, which covered the time of occurrence, an approximation of the cause, and their orbit. In this study, we focused on examining its speed (*Vsw*) between February 1 and February 12, 2022. In parallel, we also examined the variation of the solar EUV flux represented by the *F*10.7 index. This index is commonly used as an indicator of the effects of solar radiation on the earth's atmosphere.

The third step was examining the variation of IMF *Bz* and electric field *Ey* to measure the effect of solar wind on the Earth's magnetosphere. Geomagnetic storm strength is significantly driven by the interaction of a southward interplanetary magnetic field (IMF) component *Bz*, high solar wind speed (*Vsw*), and the convective electric field *Ey*. The southward IMF *Bz* enhances magnetic reconnection, allowing more solar wind energy to penetrate the Earth's magnetosphere. This energy is further increased by high solar wind speeds, while a strong *Ey* field drives enhanced currents and particle transport within the magnetosphere. Together, these factors contribute to the development and intensification of geomagnetic storms. The high variation of geomagnetic activity through geomagnetic storms can be examined through some indices, such as *AE*, *Dst*, and *Ap*, which is the concern of the fourth step. Here, we utilized the *Ap* index, together with the F10.7 index, to investigate the changes in species densities in the atmospheric layer using the NRLMSISE-00 model. The changes in species densities give rise to an increase in drag around the LEO satellite, affecting its altitude.

In the last step, we examined how magnetic storms affected total electron content (TEC), a measurement of the plasma instability that impacts the propagation of electromagnetic waves in the ionospheric layer between 100 and 1000 km altitude (Izurieta et al. 2022). As will be seen in the next section, we then looked at how variations in species densities and TEC affected atmospheric drag, which is closely tied to satellite altitude. In the present study, we adopted the NRLMSISE-00 model to account for composition, total mass density, and temperature in the atmosphere (Picone et al. 2002). The NRLMSISE-00 model can estimate atmospheric variation under geomagnetic conditions. However, the NRLMSISE-00 model underestimates the neutral densities during geomagnetic storms (Laskar et al. 2023; He et al. 2023). A study done by Ray et al. (2022) showed that the estimated uncertainty of NRLMSISE-00 densities is about 15% under mean conditions. The variation in species densities obtained from NRLMSISE-00, combined with the analysis of several space weather parameters, became the primary reference in finding the cause of the altitude loss of Starlink satellites. The comparison between two cases (decay and non-decay) also presented in this manuscript.

2 Results and discussion

2.1 Results

The data from all Starlink satellites will be analyzed in the present paper. All satellites were launched on February 3, 2022. The total mass of the Starlink satellites is 260 kg, and they are orbiting at an average altitude below 300 km with an inclination of about 53 deg. They travel at an average orbital speed (*V*) of approximately 7.5 km/s. To calculate the drag force, it is assumed that the drag coefficient (C_D) is typically around 2.2 and that the cross-sectional area (*A*) of Starlink satellites is approximately 15.45 m^2 (Hardy 2020). We attempted to examine the decay of altitude on Starlink satellites using the Two Line Element (TLE) data, providedby Space-Track (2022) at(https://www.space-track.org). The north american aerospace defense command (NORAD) TLE sets have already been generated with a few orbit propagator models, one of which is SGP4 (Simplified General Perturbations 4), and which already include the secular effects of gravitation and atmospheric drag (Hoots and Roehrich 1980; Picone et al. 2005). The theory employed in SGP4 ought to be a good representation of the state of mathematics today (Vallado et al. 2006). In this study, satellite positions like latitude, longitude, and altitude were obtained using the TLE data and then updated using the SGP4 model. The species densities along the satellite's trajectory were then calculated using the satellite's position as an input to the NRLMSIS-00 model. Examining the TLE data for all Starlink satellites, we found that only six of the seventeen satellites decayed during the analysis period, which was from February 1–12, 2022, while the other satellites were still classified as active satellites. We deliberately present data from all satellites of that launch tabulated in Table 1.

The satellites decayed at different times, as shown in Table 1, but all decays occurred between February 6 and February 12, 2022. It is known that a magnetic storm occurred in the preceding period, around February 3–4 (Kataoka et al. 2022; Bojilova and Mukhtarov 2023), affecting the satellite's orbital environment. However, not all Starlink satellites undergo orbital decay. To examine the impact of geomagnetic disturbances on the Starlink satellites, we attempted to investigate several parameters, which were divided into three groups, as shown below.

1. The perigee altitude of Starlink satellites.
2. Geomagnetic storms are attributed to space weather parameters such as the *Ey*, *Vsw*, *Bz*, *Dst*, and *AE* indices.
3. Solar EUV flux and species densities, such as the density of O, O_2, and N_2 along the satellite's trajectory, were generated from the NRLMSISE-00 model.

Table 1 Data for Starlink satellies was used in the present study

No	Object ID	Apogee (km)	Perigee (km)	Period (minutes)	Launch	Status	Decayed time
1	51456	164	144	87.56	Feb 3	Decayed	Feb 6
2	51457	303	202	89.55	Feb 3	Decayed	Feb 8
3	51458	271	192	89.13	Feb 3	Decayed	Feb 6
4	51459	287	192	89.3	Feb 3	Decayed	Feb 7
5	51460	311	278	90.41	Feb 3	Active	–
6	51461	314	285	90.5	Feb 3	Active	–
7	51462	313	285	90.5	Feb 3	Active	–
8	51463	312	279	90.42	Feb 3	Active	–
9	51464	313	284	90.49	Feb 3	Active	–
10	51465	314	284	90.5	Feb 3	Active	–
11	51466	241	185	88.75	Feb 3	Decayed	Feb 9
12	51467	541	539	95.44	Feb 3	Active	–
13	51468	540	539	95.44	Feb 3	Active	–
14	51469	541	539	95.44	Feb 3	Active	–
15	51470	167	147	87.62	Feb 3	Decayed	Feb 12
16	51471	520	519	95.01	Feb 3	Active	–
17	51472	541	539	95.44	Feb 3	Active	–

In the first group, we presented the evolution of perigee altitude for all Starlink satellites listed in Table 1. Since most satellites were launched at the beginning of February 2022, the time from their launch until decay was short, which is less than 7 days, so their orbital evolution data, specifically perigee altitude, was not much gained. Here, we only displayed the variation of perigee altitude for several-day interval data, as shown in Fig. 2.

Figure 2 depicts the evolution of the orbital height (colored-dashed line) of the six decaying Starlink satellites. Due to the limited orbital data available, we can only simulate the evolution using generated TLE data from the SatEvo v0.51 program (developed by Alan Pickup). The required parameters for the program were selected to closely match the reentry dates reported by SpaceTrack. As previously mentioned, SpaceTrack only presented the TLE data from February 5, so the evolution of the satellite's altitude from its launch on February 3 to February 4 cannot be displayed. For instance, in the case of the decay of some Starlink satellites such as #51457, #51458, #51459, and #51466, there were only three TLE datasets available in SpaceTrack, which were not enough to display the evolution of their perigee altitudes. The use of the SatEvo v0.51 program in Fig. 2 is just to show the evolution of perigee altitudes for each Starlink satellite. We noticed that SatEvo v0.51 used the last TLE set of each Starlink satellite in addition to current solar activity data for the actual re-entry forecast. The accuracy of the SatEvo v0.51 simulation affects the uncertainty of the re-entry window. We should point out that in the present study, we did not perform a simulation to predict the re-entry window of all decaying Starlink satellites. We also did not use SatEvo v0.51 for the purpose of analysis, especially in its relationship with geomagnetic storms and changes in atmospheric densities.

In Fig. 2, we can see that the decay of each satellite did not occur at the same time, as not all of them re-entered the atmosphere on February 8 (days of year/DOY 39). For instance, the orbital decay of the Starlink #51456, #51457, #51458, and #51459 satellites occurred during February 6–8, 2022, whereas Starlink #51466 and #51470 decayed during February 9–12, 2022. The perigee altitudes of most decaying satellites were less than 200 km. The 200 km altitude is assumed to be a starting point to predict a short-term re-entry (Klinkrad 2006). In contrast to the decay of Starlink satellites that were launched in the first batch, those that were launched in the second batch of the month (black-dashed line) did not show the same decrease in their orbital altitudes as in the case of decaying Starlink satellites. We suggested that there are two reasons for this, i.e., 1. This is due to their much higher initial altitude (lessons to be learned from the accident), in which the atmospheric drag insignificantly affected their orbit; and 2. They were located at a different local time than all decaying Starlink satellites, where the effect of substoms could be negligible. Regarding the first reason mentioned above, the Starlink team has attempted to prevent the effect of increased drag on the orbit of the Starlink satellites by commanding the satellites into a safe mode. Unfortunately, some satellites with lower perigee altitudes had to reenter the atmosphere because the increased drag prevented them from leaving safe mode

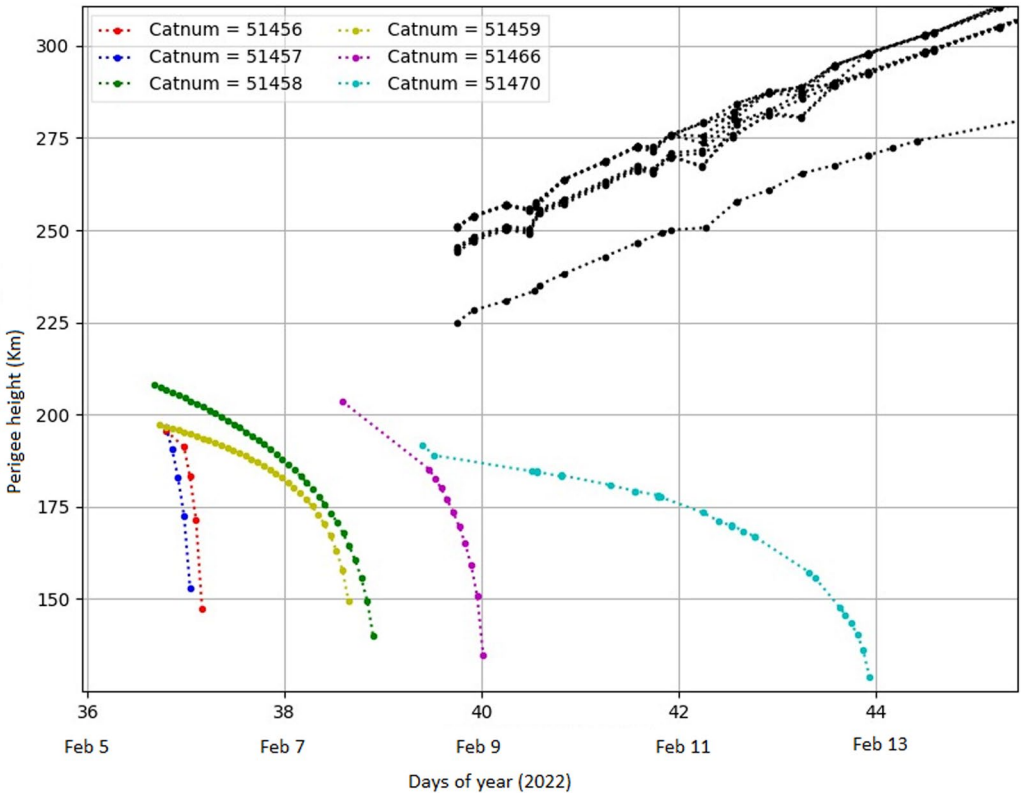

Fig. 2 The evolution of perigee altitude for all Starlink satellites in February 2022. The ones that decayed (displayed in different colors) are from the earlier batch of the month, while the black dashed lines represent some of the satellites from the later batch that were injected at higher altitudes to prevent similar accidents (Fang et al. 2022)

to start orbit-raising maneuvers, as described by Satnews (2022) at (https://news.satnews.com/2022/02/13/starlink-satellite-loss-explained/). The remaining satellites with higher perigee altitudes were insignificantly affected by increased drag and could be controlled to avoid decay.

To find the relation between the decay of Starlink satellites and their environmental parameters, we first analyzed solar wind speed (V_{SW}) and the north–south direction of the interplanetary magnetic field (IMF Bz), since both parameters have strong relationships with variations in the Earth magnetosphere, leading to geomagnetic storms (Lakhina et al. 2006). In Fig. 3A, we clearly see that the average speed of the solar wind increased within three clusters, i.e., during February 3–4 (DOY 34–35; $V_{SW} \sim 575$ km/s), February 5–6 (DOY 36–37; $V_{SW} \sim 590$ km/s), and February 12 (DOY 43; $V_{SW} \sim 565$ km/s). It is noteworthy that the variation in solar wind speed can affect the Earth's magnetosphere radius by ± 20% (Russell 2001). The coupling between the solar wind and the southward interplanetary magnetic field ($Bz < 0$) can result in reconnection with the Earth's magnetosphere (Lakhina et al. 2006). In Fig. 3B, the southward IMF with $Bz < -5$ nT occurred within three clusters, i.e., February 3 (DOY 34; $Bz \sim$ --18 nT), February 4 (DOY 35; $Bz \sim -9$ nT), and February 10 (DOY 41; $Bz \sim -12$ nT). The average southward IMF with $Bz < -5$ nT for each cluster lasted 5 h. It is known that if the IMF $Bz < -3$ nT occurs for one hour, it can trigger the magnetic substorms (Kamide et al. 1977).

The interaction between solar wind (V_{SW}) and southward IMF Bz also gives rise to the induced electric field Ey shown in Fig. 3C. Here, the enhanced electric field Ey occurred with the same cluster as IMF Bz. The maximum Ey in the first (February 3; DOY 34) and last cluster

(See figure on next page.)

Fig. 3 Variation of environmental parameters in the period of Starlink satellite orbital decay. The black arrows indicate high fluctuations of each environmental parameter for **A** Solar wind speed (Vsw), **B** IMF Bz, **C** Interplanetary electric field (Ey), **D** Dst and AE indices, **E** Ap index, and **F** Solar EUV flux (F10.7) (Hardy 2020)

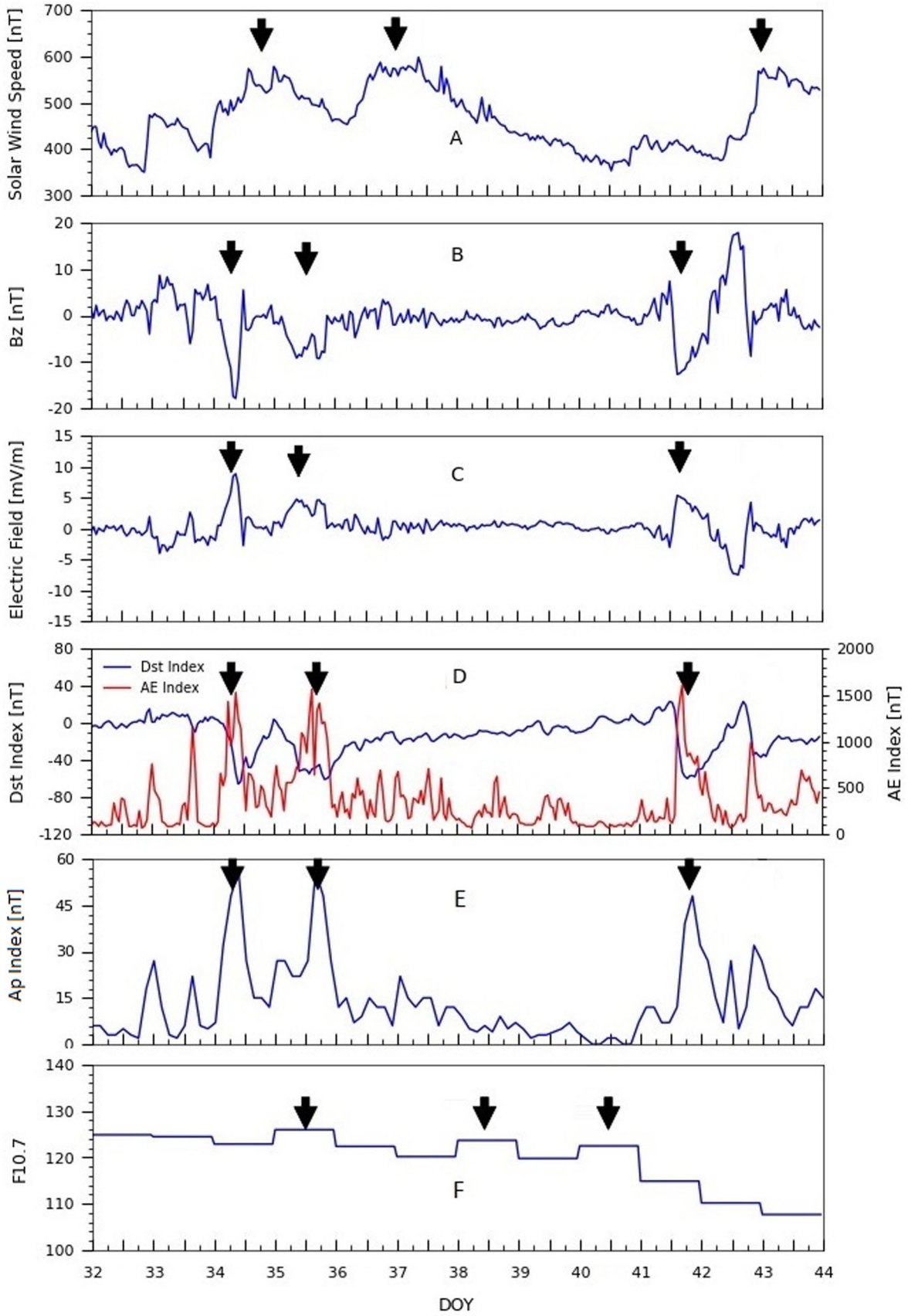

Fig. 3 (See legend on previous page.)

(February 10; DOY 41) is greater than 5 mV/m, whereas the second cluster (February 4; DOY 35) is lower than the two, which is around 4.5 mV/m. We can see that the electric field *Ey* varies coincidentally with the IMF *Bz* variation, but in the opposite pattern. The production of geomagnetic storms and substroms has been found to be correlated with the electric field *Ey* (Nikolaeva et al. 2011). The drop of IMF Bz and an increase of Ey occurred on the day of the launch of Starlink satellites. Compared to the previous days (DOY 32–33), the drop of IMF *Bz* and the rise of *Ey* on DOY 34 (Starlink launch) reached around 60% and 87%, respectively. These values were obtained by averaging IMF *Bz* and *Ey* during < DOY 34 and then comparing them to the average values calculated during DOY 34.

The coupling of rapid solar wind and southward IMF *Bz* is obviously effective in giving rise to magnetic reconnection, as indicated by the increase in interplanetary electric field (*Ey*) shown in Fig. 3C. During reconnection, a large number of energetic particles from solar winds penetrate the inner magnetosphere through the polar cusps and are then stored in the earth's magnetotail, reaching the ionospheric layer of the earth. The transferred energy can be released during geomagnetic substorms, leading to enhanced currents in the magnetosphere and ionosphere. The intensity of currents can be indicated by the rise of both the *AE* and |*Dst*| indices. This explains that the increase of *AE* and the drop of *Dst* in Fig. 3D are strongly related to the *Ey* variation. Both *AE* and *Dst* have a similar cluster of storms, i.e., February 3 (DOY 34; $AE \sim 1530$ nT & $Dst \sim -66$ nT), February 4 (DOY 35; $AE \sim 1560$ nT & $Dst \sim -61$ nT), and February 10 (DOY 41; $AE \sim 1613$ nT & $Dst \sim -58$ nT). We tried to count the time difference (Δt) between the "peaks" of AE and "valleys" of Dst for the three clusters. We found that the Δt for each cluster varied, i.e., February 3(DOY 34; $\Delta t \sim 1$ h), February 4 (DOY 35; $\Delta t \sim 4$ h), and February 10 (DOY 41; $\Delta t \sim 2$ h). The average time delays for the three clusters are less than 5 h, indicating that the fluctuation of the electric field affects both polar and ring current regions with short time delays (< 5 h) between the "peaks" of *AE* and "valleys" of *Dst*. The moderate-scale geomagnetic storms that occurred at the beginning of February 2022 seemed effective enough to change the ambient plasma in both polar and ring current regions.

Since atmospheric molecules are strongly affected by geomagnetic activity, the use of *Dst* and *AE* indices to describe the level of geomagnetic storms impacting the atmospheric layer is very important for analysis. As previously mentioned, the *Dst* index (Fig. 3D, blue) represents the occurrence of magnetic storms in the equatorial (ring current) region, whereas the auroral electrojet (AE) index (Fig. 3D, red) characterizes auroral, high-latitude magnetic activity attributed to increased ionospheric currents (Burton et al. 1975). During magnetic storms, energetic particles from high latitudes and ring currents can move to lower latitudes. This particle drift is caused by several mechanisms, including the electromagnetic ion cyclotron (EMIC) (Yuan et al. 2018) and the Whistler mode chorus (Horne et al. 2005), both of which are important in electron transport at low altitudes.

At least three substorms were discovered during the analysis period, beginning with two successive substorms before February 5 (DOY 36) and ending on February 10 (DOY 41), as shown in Fig. 3D. This is demonstrated by a rapid drop in the *Dst* index and a sharp rise in the *AE* index. The presence of several substorms implies unstable magnetic conditions, particularly in the radiation belt inhabited by energetic particles. The electrojet activity of the auroral oval region affects the properties of the particles in the ring current connected by the field align current during the main phase of the geomagnetic storm (Gonzalez et al. 1994). Under these conditions, successive substorm events disrupt the particle population's stability until the accumulation of these particles is then transported closer to Earth by an electric field generated by a magnetic field (Kamide 1992; Lakhina et al. 2006).

We further investigated the influence of magnetic substorms on the environment around the Starlink satellites. When a substorm occurs, a large number of particles reach the atmospheric layers. During southward IMF, the higher the solar wind speed, the larger the electric field affecting the magnetospheric layer. In Fig. 3D, a moderate-scale substorm ($Dst < -50$ nT, lasted 3 h) occurred on the same day as the launch of Starlink satellites, which was February 3 (DOY 34). Subsequent substorms occurred on February 4 (DOY 35) and 10 (DOY 41), with longer durations of around 6 and 8 h, respectively. The effect of this magnetic substorm induced a change in ionospheric electric current, where the *AE* index dramatically rose to above 1000 nT three times, two before and one after February 8 (DOY 39). Figure 3D displays an increase in ionospheric currents with arrows.

We then looked at the daily *Ap* index to establish the influence of magnetic subtorms on atmospheric layers. It is known that the NRLMSIS-00 empirical atmospheric model estimates its species densities, one of which is a function of the daily *Ap* index (Picone et al. 2002). The enhanced *Ap* index also occurred within three clusters, similar to the *Dst* and *AE* clusters, i.e., February 3 (DOY 34; $Ap \sim 56$ nT), February 4 (DOY 35; $Ap \sim 56$ nT), and February 10 (DOY 41; $Ap \sim 48$ nT). A geomagnetic storm is typically identified when the *Ap* index is greater than 30 nT (Hastings and Garrett 2015). The variation in atmospheric density for orbital decay rate calculation is specified as a function

of the *Ap* index (Kennewel 1999). All clusters showed the *Ap* index significantly increased up to 50 nT, which strongly inferred the instability of the atmospheric layer due to substorms. The average peak of *Ap* lasted for about 2 h. This is counted through the width of the peak in each cluster shown in Fig. 3E.

We examined the impact of solar radiation on atmospheric drag using the solar radiation flux at 10.7 cm (2800 MHz) depicted in Fig. 3F, notwithstanding the magnetic contribution to variations in atmospheric layers. The *F*10.7 index ranges from roughly 50 sfu at the solar minimum to 240 sfu at the solar maximum (Hastings and Garrett 2015). The *F*10.7 index is also used to specify the species density in the NRLMSISE-00 model in addition to estimating atmospheric drag, which results in the orbital decay of satellites (Kennewel 1999). A quick increase in molecular density gives rise to changes in atmospheric drag that can lead to a significant decrease in satellite altitude. The radiation flux rose on multiple occasions with an index value larger than 120 sfu (Fig. 3F). The amount of solar energy that air molecules absorb decreases with altitude and is significantly less than that of molecules dispersed over 200 km (Prolss 2004). Interestingly, the *F*10.7 maxima for the three clusters occurred on February 5 (DOY 36; *F*10.7 ~ 126 sfu), February 7 (DOY 38; *F*10.7 ~ 124 sfu), and February 9 (DOY 40; *F*10.7 ~ 123 sfu), which is different from the peak times for the magnetic clusters and tends to decrease over the course of the analysis. The cause of this difference is beyond the scope of this study. However, we found a similar pattern in which the *F*10.7 peaks corresponded to the *AE* peaks but occurred at different times. We tried to look at *F*10.7 index data prior to February, and we noticed that the index had been continuously rising from January 25 through January 30 (~ 18%) before dropping slightly until February 2 (DOY 33). On the day of the Starlink launch, the *F*10.7 index slightly rose again. This increase fluctuated slightly up to February 10 (DOY 41) and then dropped significantly, as shown in Fig. 3F. The early peak of the *F*10.7 index coincided with the launch of Starlink satellites (February 3; DOY 34). Comparing the two conditions—quiet days before January 25 and disturbed days, which began to increase after January 25—this index increased significantly—from an average of 93 sfu (quiet) to an average of 118 sfu (disturbed). Overall, the increase in *F*10.7 from January 25 to the time before *F*10.7 dropped significantly (February 10; DOY 41) was around 27%. Here, we inferred that the impact of solar EUV flux on species densities is assumed to be relatively considerable because, apart from experiencing a continuous increase, the peak of the *F*10.7 index was found to be more than 120 sfu (mild) on some occasions. We will show this impact on densities in the next section.

The variation of solar EUV flux and geomagnetic storms strongly depends on solar activity. During periods of high solar activity, a large number of energetic particles were injected through the solar wind into the magnetosphere, and a portion of them penetrated the upper atmosphere, causing changes in plasma properties such as an increase in temperature and density. Changes in plasma properties around satellite altitude have a direct impact on the loss of orbital energy for orbiting satellites. This is because the spacecraft undergoes a drag force in the opposite direction to its orbital motion, so the changes in atmospheric density will affect the changes in satellite velocity, as explained through the following equation:

$$v = \sqrt{\frac{2F}{\rho A C_D}} \tag{1}$$

Here F represents the drag force acting on the spacecraft (N), ρ is the atmospheric density (kg/m^3), A is the cross-sectional area of the spacecraft (m^2), and C_D is the drag coefficient (typically $C_D = 2.214 \pm 0.043$). In general, this formula is obtained by transforming aerodynamic force generated through momentum exchange between the atmosphere and the satellite. The effect of drag on a spacecraft's orbit can be determined through the rate of change of energy of the spacecraft (*dE/dt*) and the rate of change of the semimajor axis (*da/dt*). Since the rate of change of energy (*dE/dt*) depends on some parameters such as atmospheric density (ρ), the cross-sectional area of spacecraft (A), and spacecraft velocity (v), the rate of change of the semimajor axis (*da/dt*) also depends on the aforementioned parameters. The details of how to get this formula can be seen in detail in Pisacane (2008). We should point out that Eq. (1) expresses the relationship between the drag force and the density and does not indicate the relationship between velocity and density. However, from this relationship we can infer that as the density of the atmosphere increases, the more particles the satellite encounters as it moves through space, increasing the drag force.The increased drag leads to the motion of satellites becoming slower. The lower the speed of the orbiting satellite, the less mechanical energy it has, leading the orbit to get smaller. The continuous energy decrease causes a loss of the satellite's altitude, driving the satellite to enter the earth's atmosphere (atmospheric re-entry). Here, the secular perturbation due to atmospheric drag is being assessed using the first order of the following equation (Klinkrad 2006; Pisacane 2008)

$$\frac{da}{dt} \approx -C_D \frac{A}{m} \rho a v \tag{2}$$

The rate of decreasing altitude (semimajor axis) depends on the ballistic parameter B ($B = C_D \frac{A}{m}$) and the increasing drag shown by Eq. (2).

As previously explained, the increased drag is caused primarily by the heating of the thermospheric layer by extreme ultraviolet (EUV) radiation and solar winds generated by the sun. During an active condition, the energy from both types of radiation is dissipated as it reaches the thermospheric layer through the Joule heating and ionization processes. Here, the impact of solar radiation has a period of around 8 min to reach the Earth. In contrast to electromagnetic radiation, charged particles from solar winds travel and reach the Earth with time delays of 1–5 days, depending on their speed. The impact of solar wind on Earth can be determined by observing its interaction with the magnetic field and using indices like *Dst*, *AE*, and *Ap*, as already shown above.

Figure 4 displays density variations along the orbital trajectory of several Starlink satellites. We analyzed some species, such as oxygen (O and O_2) and nitrogen (N_2) during the decay of Starlink satellites, as shown in Fig. 4 (left panel). We see the comparisons of molecular density changes in decaying Starlink cases (e.g., Starlink #51456, #51458, #51466) and non-decaying Starlink cases (e.g., Starlink #51460, #51461, #51465). The red and blue lines represent oxygen fluctuations (O and O_2, respectively), and the green line represents N_2 variations. It should be noted that these variances are based on changes in the height of the Starlink satellite orbit over the course of the analysis. The molecular densities for O and O_2 rose during the analysis interval in the decaying cases (left panels). In the non-decaying cases, however, there were no notable changes in the air molecule densities (right panels), indicating that all of the observed molecular densities fluctuated naturally. Here, we indicated that the increase of O and O_2, can be a good indicator to estimate an increasing or decreasing drag in the thermospheric layer (Fig. 5), which can reduce the height of the satellite as experienced by some Starlink satellites.

In Fig. 5 (left panel), we can see that during the decay of Starlink satellites, the drag force along the satellite's trajectory rose as the orbital altitude declined, following an increase in species densities in Fig. 4 (left panel). On the other hand, for non-decaying Starlink cases (Fig. 5, right panel), the drag force insignificantly changed over the time considered. Here we displayed the plot of drag force on the logarithmic scale, which varied from around 5.10^7–$6.3.10^7$ N.

In order to examine the significance of geomagetic storms, represented by the *Ap* index, and solar EUV flux,

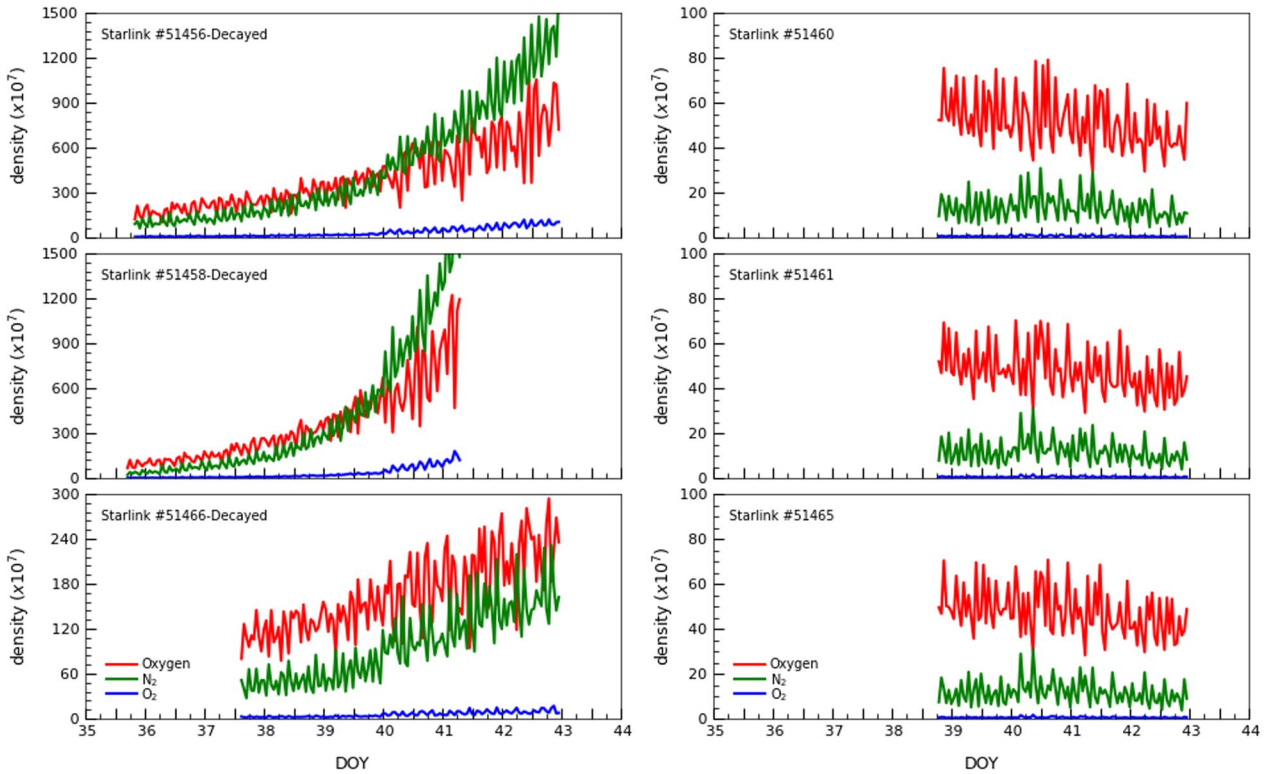

Fig. 4 Variation of molecular densities for all species in the atmosphere in the period of February 1–12, 2022. We only presented three cases for decaying Starlink (left panel) and three cases for non-decaying Starlink (right panel) as examples (Kennewel 1999)

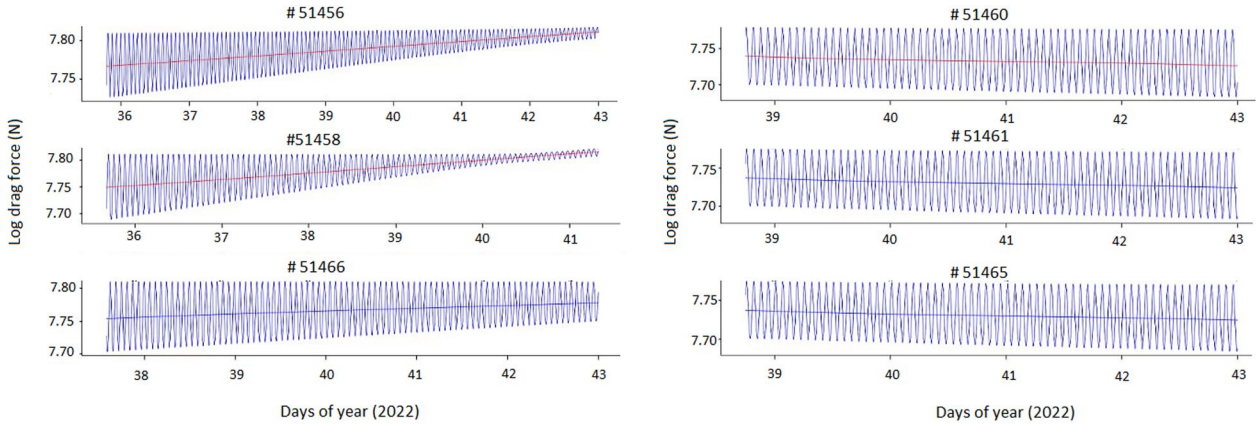

Fig. 5 Variation of atmospheric drag along the satellite's orbit for the decay of some Starlink satellites (left panel) and for non-decaying Starlink satellites (right panel) as examples. The y-axis in this figure represents the drag force on a logarithmic scale (Klinkrad 2006)

represented by the *F*10.7 index, we attempted to find a correlation coefficient (*r*) between total mass density, obtained from NRLMSISE-00, and both the *Ap* and *F*10.7 indices. Here, we averaged the hourly values of each parameter to get their daily values for the time period of January 20 to February 20, 2022. We intentionally extended the duration of the analysis to fit more data. The total mass density fluctuation was measured at a height of 200 km. The reason why we took samples at an altitude of 200 km is because the short-term re-entry prediction starts at approximately 200 km perigee altitude (Klinkrad 2006). The correlation coefficient was obtained after binning the *Ap* and then fitting the line for the averages of *Ap*. The correlation for each parameter can be seen in Fig. 6.

Figure 6A shows that there was a strong correlation between the occurrence of geomagnetic storms and their effects on the thermospheric layer, which led to an increase in total mass density with a *r* value of about 0.77 ($r=77\%$). With a *r* value of approximately 0.63 ($r=63\%$), Fig. 6B also made it clear that the effect of solar EUV flux on the thermospheric layer was slightly smaller than that of substorm occurrences.

Finally, we attempted to assess the impact of magnetic storms on the thermospheric layers by analyzing total electron content (TEC) data within the analysis timeframe. We obtained the TEC data from NASA (2022) at https://cddis.nasa.gov/archive/gnss/products/ionex/. Since TEC represents the total number of free electrons and ions that can affect electromagnetic wave propagation in the ionospheric layer, it can be a good indicator of the impact of magnetic disturbances on the ionosphere, including Starlink satellites. In addition, the ionosphere and thermosphere are closely coupled, and the use of TEC sometimes can reflect the thermospheric conditions, particularly under specific conditions like

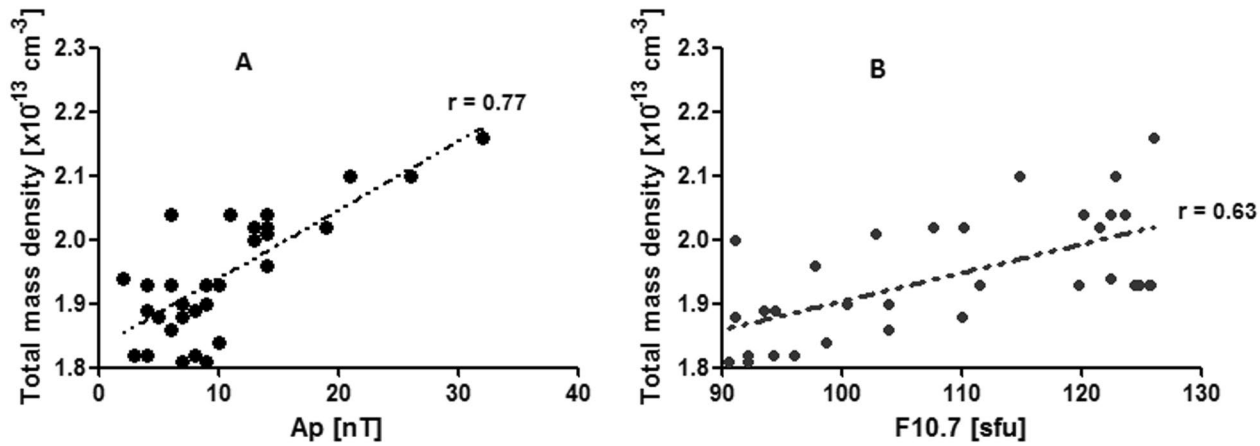

Fig. 6 The correlation coefficient between total mass density and Ap index (**A**) and total mass density with F10.7 index (**B**) during the time interval of January 20–February 20 (Klinkrad 2006)

geomagnetic storms. TEC tends to increase with higher solar flux, which also increases thermospheric heating and, consequently, the neutral density. While there is some coupling between the ionosphere and thermosphere, changes in TEC do not directly reflect changes in the neutral density that is primarily responsible for satellite drag. However, since the loss of Starlnks satellites occurred during periods of geomagnetic storms, the increase in neutral density around the Starlink satellite environment can also be reflected by the increase in TEC.

Figure 7 depicts changes in TEC caused by magnetic disturbances. We should note that we only showed TEC data in Fig. 7 for four periods: before the substorm (e.g., February 2; DOY 33), during the substorm (February 3 & 4; DOY 34 & 35), after the substorm (February 5; DOY 36), and a subsequent substorm (February 10; DOY).

Figure 7A shows that on February 2, the day before Starlink was launched, there were indications of an increase in TEC, particularly in low latitudes. Although the value of the *Dst* index has not decreased, a tendency toward an increase in the value of the *AE* index has been observed, as shown in Fig. 3D. On February 3, a new magnetic storm began and lasted until February 4. The *Dst* and *AE* indices both showed large fluctuations. Geoagnetic storms raised TEC not only at low latitudes but also at middle latitudes (Fig. 7B, C). The decrease in magnetic storm intensity was followed by a decrease in TEC, which returned to normal as shown in Fig. 7D. A subsequent storm occurred on February 10, when the *Dst* fell drastically and the *AE* increased to 1600 nT. This led the TEC to expand to the south Atlantic anomaly (SAA) and mid-latitude regions, as shown in Fig. 7D. It should be noted that this increase in TEC occurred until February 12. This suggests that, between February 1 and 12, 2022, the thermospheric layer was disturbed due to magnetic substorms, as shown by an increase in species densities like O and O_2, as well as an increase in TEC over a few days. This instability was likely what caused orbital decay on some Starlink satellites, especially those with lower altitudes. The question arose: why were only some of the Starlink satellites

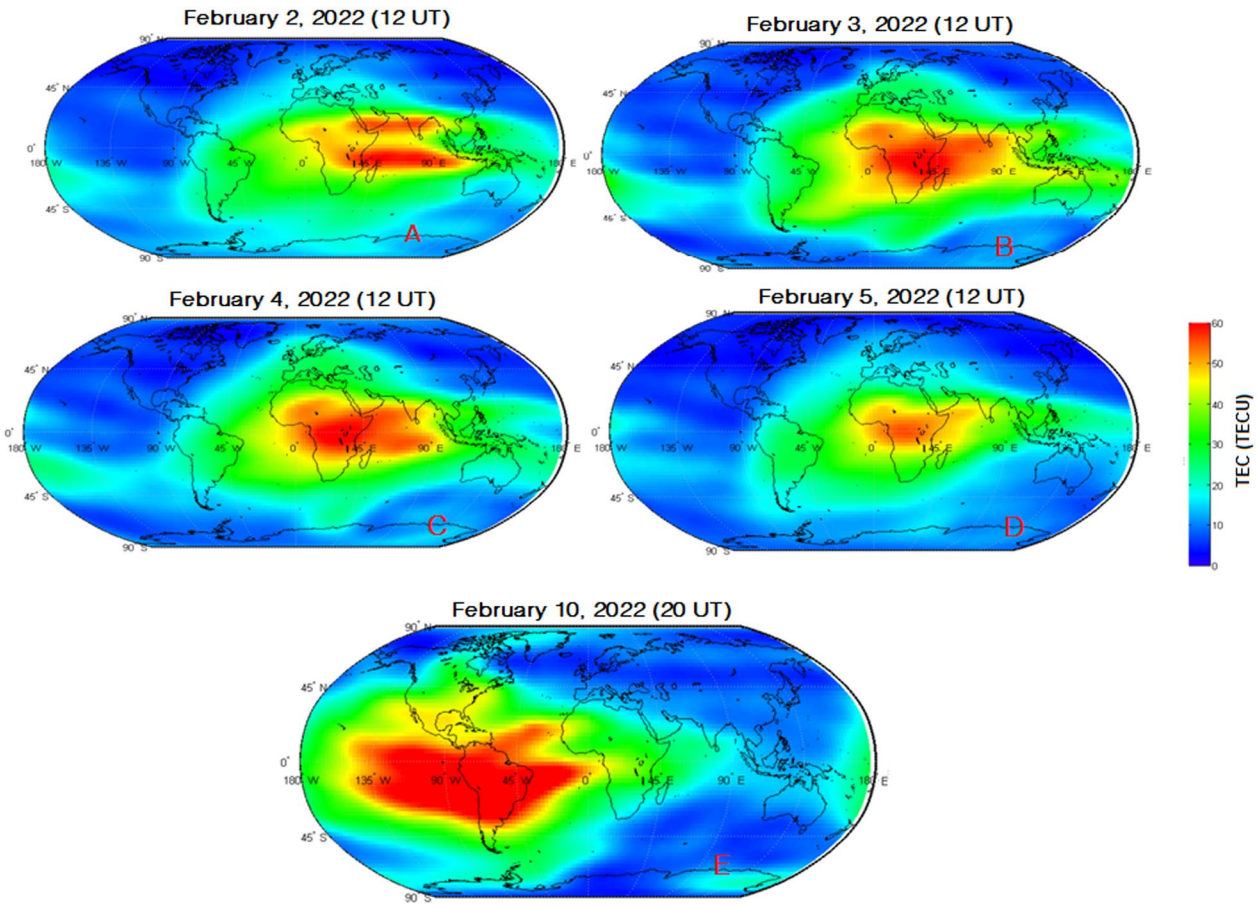

Fig. 7 Variation of total electron content (TEC) during the decay of some Starlink satellites in its relationship with geomagnetic substorms.We only presented some events as examples (Krauss et al. 2018)

affected by this magnetic storm and the others not? This will be discussed in the discussion session.

3 Discussion

To investigate why certain Starlink spacecraft decayed while others did not, we attempted to look into the position of each Starlink satellite from its launch through February 12, 2022. We prefer to utilize satellite positions in magnetic local time since it is easier to explain the occurrence of magnetic storms. The algorithm used to determine the satellite's local time is the same as that employed by Ahmad et al. (2018) and Ahmad (2020). Figure 8 depicts the local time of this satellite.

Figure 8 displays the local time and latitude of each satellite in the geomagnetic coordinate in various colors and symbols. Here, the location of each satellite in geographic coordinates is transformed into geomagnetic coordinates using the converter provided by the World Data Center for Geomagnetism (2022) at https://wdc.kugi.kyoto-u.ac.jp/igrf/gggm/. All decaying Starlink satellites (shown by colored circles) were clearly in the midnight to dawn sector of magnetic local time, while non-decaying Starlink satellites (marked by diamonds and plus colored symbols) were in the dusk to midnight sector. This variation in local time explains why some Starlink satellites decayed while others did not. This viewpoint can also explain the connection between the influence of a magnetic substorm and the deterioration of numerous Starlink satellite orbits.

An interesting study found that the magnetic storms and substorms are related to the southward Interplanetary Magnetic Field (IMF *Bz*) through the radial component of the solar wind velocity and current distribution in the magnetospheric–ionospheric system (Nikolaeva et al. 2011). The changes in currents directly affect the intensity of magnetic disturbances characterized by the *AE* and *Dst* indices (Davis and Sugiura 1966).

The majority of LEO satellites, including Starlink, are located in the upper atmospheric layer, where energetic electrons can penetrate during storms and substorms. The characteristics of the ambient plasma in this layer are directly impacted by the precipitation process. The fact that the mechanisms causing electron precipitation into the atmosphere varied for various energy ranges is intriguing. For instance, energy less than 10 keV is associated with the discrete aurora due to the interaction between wave and particle around the magnetic equator, whereas energy greater than 30 keV is linked to the

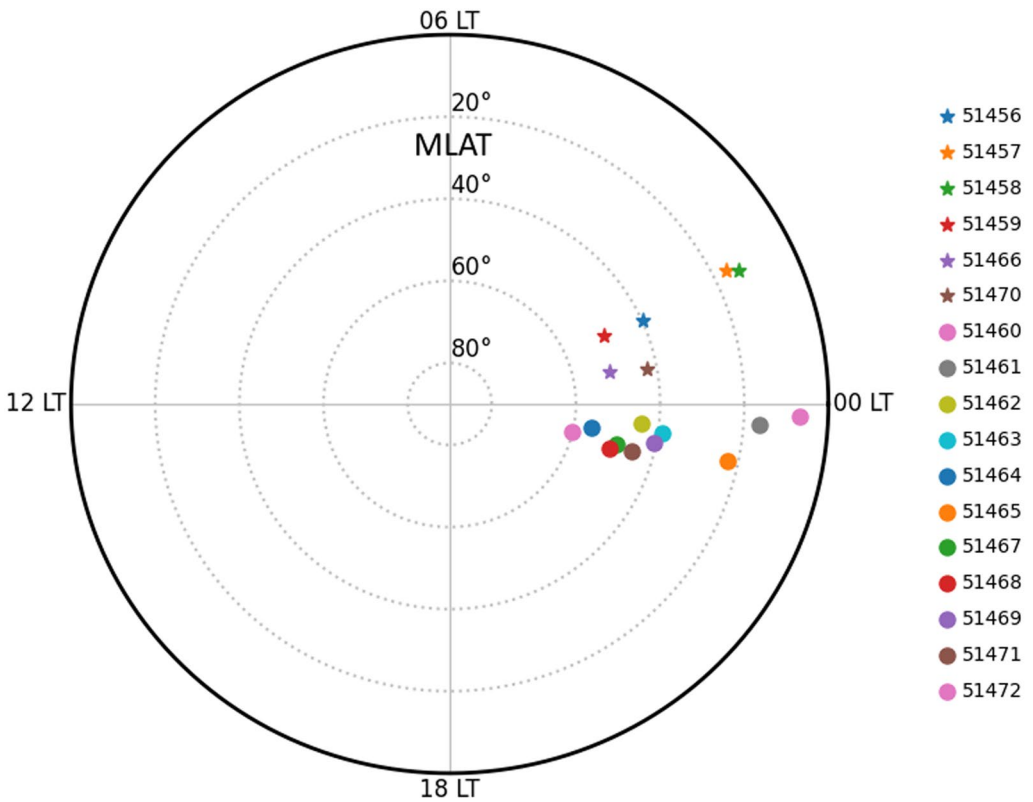

Fig. 8 Position of Starlink satellites in terms of satellite local times within the period of their launch to February 12. All satellites resided in the night sector of magnetic local time, but in different subsectors (Lam et al. 2010)

wave-particle interaction in the Van Allen radiation belts through whistler mode chorus waves (Lam et al. 2010).

It is evident from the present analysis that there was a very active state where the *AE* index quickly rose to more than 500 nT, particularly at the beginning of February 2022. A large number of electrons were likely transported from the magnetotail and then precipitated into the ionospheric layer through auroral field lines, giving rise to an increase in the AE index. The disturbance of the thermospheric layer, especially in the polar region, is associated with particle population changes in the magnetotail lobe and plasma sheet, which then produce electric fields in the polar upper atmosphere. The transverse of electric fields leads to ambipolar ExB drift of the charged particles in the thermospheric layer (Prolss 2004). The flow of currents in the polar region can be divided into two directions, i.e., westward in the dawn sector and eastward in the dusk sector. It is found that an equatorward polarization electric field is often produced by the electrical conductivity of the ionosphere, which has a peak close to the auroral oval's equatorward boundary. Field-aligned currents are generated when the electric field's space charges are free to enter the magnetosphere under quiet conditions. During geomagnetic storms, the convective electric field is increased, leading to the growth of field-aligned currents. As a result, the magnetosphere's Hall current is unable to close freely, which causes a significant accumulation of space charges close to the oval's equatorward boundary. The resulting polarized electric field drives the transport of plasma toward the magnetopause in the dawn sector, stimulates the expansion of the westward electrojet, and generates an intense westward current (Coroniti and Kennel 1971; Akasofu 1977).

Other explanations are related to the temperature increment during geomagnetic storms, as shown through some studies. Burns et al. (1995) performed a simulation that revealed the typical vertical winds under quiet geomagnetic activities, which are upward in the afternoon and late-evening sector and downward in the night-dawn sector of magnetic local time. High latitude energy deposition disrupts the typical thermospheric equator-to-pole circulation during geomagnetic storms. Due to the pole-to-equator circulation under such modified conditions, the dawn-sector vertical winds at low- and mid-latitudes become increasingly downward, enhancing compressional heating in comparison to quiet time. On the other hand, the circulation due to geomagnetic storms weakens the vertical winds in the dusk sector, which reduces thermosphere expansion and decreasing temperature. This explains why the temperatures in the dawn sector, during geomagnetic storms, are greater compared to the dusk sector. This finding is further confirmed by Laskar et al. (2021) using temperature data derived from the Global-scale Observations of Limb and Disk (GOLD) disk measurements.

It is evident that the drag force experienced by a satellite, apart from depending on the satellite's cross-sectional area and velocity, also depends on neutral density. The higher the neutral density, the more particles the satellite encounters as it moves through space, increasing the drag force. During periods of geomagnetic storms, the temperature increases, and the gas at the thermosphere gains more kinetic energy, causing the atmospheric heats up and expands, increasing the neutral density at a given altitude. This leads to increased drag on satellites, causing them to lose altitude more quickly. As previously mentioned, Burns et al. (1995) and Laskar et al. (2021) found that the thermospheric temperature at the dawn sector was higher than that at the dusk sector. Given that temperature and neutral density are strongly correlated, the increased drag in the dawn sector could be responsible for the decay of the Starlink satellites in the dawn sector.

4 Conclusion

We conducted an investigation into the causes of altitude loss on Starlink satellites. This analysis referred to a SpaceX report that as many as 40 of 49 Starlink satellites experienced decay, which is thought to be related to the magnetic storm that occurred on February 4, 2022. The decay of Starlink satellites was reported on February 8, approximately 5 days after launch. However, we only found that 17 Starlink satellites, which were launched on February 3, were registered in the SpaceTrack database, which is the basis for the present analysis. To ascertain the presumed cause of satellite decay, we attempted to analyze many parameters shown in Figs. 3, 4, 5, 6, 7, 8. We found significant variations in all the features we examined. The high speed of the solar wind and a decrease in the value of *Bz* caused an increase in the electric field *Ey* in the magnetosphere. The increase in the electric field *Ey* leads to ExB drift of the charged particles, giving rise to a depression of the *Dst* value and an increase of the *AE* value. It is also found that solar EUV flux increases, together with an increase in ionnospheric currents (represented by the *AE* index), affecting the species densities in the thermospheric layer.

In the decaying Starlink cases, all species densities, such as O, N_2, and O_2, experienced an increase, whereas in the non-decaying Starlink cases, those species densities did not change much. We should point out that the increased species densities in the case of decayed Starlink satellites shown in Fig. 4 not only come from geomagnetic storm impact but also due to the declining altitude of Starlink satellite orbits. Increasing densities occurred around DOY 34 after geomagnetic storms. Most

decaying satellites have already reentered the atmosphere before DOY 40. We suggested that the increased species density after DOY 40 was not solely related to geomagnetic storm impact but rather to the declining altitudes of Starlink satellites. The contribution of solar EUV flux and geomagnetic activities on changes in species densities can be seen through the correlation coefficient (r), where both parameters showed significant r values around 77% for geomagnetic and 63% for solar EUV contributions. In addition, we discovered multiple instances of the TEC value increasing over the time considered. We presumed that numerous Starlink satellites started to disintegrate during this time due to thermospheric layer disturbances.

The question that arose was why only some of the Starlink satellites experienced decay and others did not. This can be answered by looking at the satellite local time of each satellite, as shown in Fig. 8. All decaying Starlink satellites were distributed in the midnight-to-dawn sector, where magnetic substorms caused the drift of ionospheric currents, which was driven by westward electrojets. On the other hand, all non-decaying Starlink satellites resided in the dusk to midnight sector of magnetic local time, where the intensity of magnetic disturbances tended to be undisturbed or experienced small disturbances that did not have a significant impact on Starlink satellites.

Abbreviations

LEO	Low earth orbit
GEO	Geosynchronous earth orbit
CMEs	Coronal mass ejections
CIRs	Corotating interaction regions
CHAMP	Challenge mini-satellite payload
GRACE	Gravity recovery and climate experiment
NOAA	National oceanic and atmospheric administration
IMF	Interplanetary magnetic field
Dst	Disturbance storm time
AE	Auroral electrojet
EUV	Extreme ultraviolet
Sfu	Solar flux units
TEC	Total electron content
NASA	National aeronautics and space administration
NRLMSIS	Naval Research Laboratory Mass Spectrometer and Incoherent Scatter Radar
TLE	Two Line elements
NORAD	North American Aerospace Defense Command
SGP4	Simplified General Perturbations 4
DOY	Days of year
AE	Auroral electrojet
EMIC	Electromagnetic ion cyclotron

Author information

All authors work for the National Research and Innovation Agency (BRIN) in the field of space environment and space debris and have performed various numerical simulations attributed to environmental effects on satellites.

Acknowledgements

The main author would like to thank the Aeronautics and Space Research Organization (ORPA)-National Research and Innovation Agency (BRIN) for providing facilities and other support for this research. We would also like to thank Telkom University, which has partially funded this publication. Finally, the authors would also like to thank SpaceTrack and NASA for providing valuable data for research.

Author contributions

NA contributed to the research, data processing, and writing of the manuscript. LOMM, HFR, and AR contributed to the programming, simulation, and processing of TLE, magnetic, and NRLMSISE-00 data. N, AH, and HFT contributed to the processing of the TEC data, manuscript, and figure preparation.

Funding

This research has been facilitated by the BRIN program and partially supported by Telkom University.

Availability of data and materials

The data considered in this study are available at https://drive.google.com/drive/folders/1-2BQjgk6jR7ug0TWxRSVGjujZ1mhVPtu?usp=drive_link.

Declarations

Ethics approval and consent to participate

Not applicable.

Consent for publication

Not applicable.

Competing interests

The authors declare that they have no competing interests.

Author details

[1]Center for Space Research, Aeronautics and Space Research Organization (ORPA), BRIN, Bandung, Indonesia. [2]Pontianak Botanical Garden, BRIN, Siantan, Mempawah 78362, Indonesia. [3]School of Industrial Engineering Telkom University, National Research and Innovation Agency of Republic Indonesia, Bandung, Indonesia. [4]Mount Timau National Observatory, BRIN, Bitobe, NTT, Indonesia.

Received: 4 September 2024 Accepted: 12 December 2024
Published online: 13 January 2025

References

Ahmad N (2020) Determination of mean local time on the day of the anomaly on LEO spacecraft. J Phys Conf Ser 1523:012003. https://doi.org/10.1088/1742-6596/1523/1/012003

Ahmad N, Herdiwijaya D, Djamaluddin T, Usui H, Miyake Y (2018) Diagnosing low earth orbit satellite anomalies using NOAA-15 electron data associated with geomagnetic perturbations. Earth Planets Space 70(1):91. https://doi.org/10.1186/s40623-018-0852-2

Akasofu S-I (1977) Physics of magnetospheric substorms. Astrophysics and Space Science Library, Springer Dordrecht, Holland. https://doi.org/10.1007/978-94-010-1164-8

Berger TE, Dominique M, Lucas G, Pilinski M, Ray V, Sewell R, Sutton EK, Thayer JP, Thiemann E (2023) The thermosphere is a drag: the 2022 Starlink incident and the threat of geomagnetic storms to low earth orbit space operations. Space Weather 21(3):1–15. https://doi.org/10.1029/2022SW003330

Billett DD, Sartipzadeh K, Ivarsen MF, Iorfida E, Doornbos E, Kalafatoglu Eyiguler EC, Pandey K, McWilliams KA (2024) The 2022 Starlink geomagnetic storms: global thermospheric response to a high-latitude ionospheric driver. Space Weather 22(2):1–16. https://doi.org/10.1029/2023SW003748

Bojilova R, Mukhtarov P (2023) Comparative analysis of global and regional ionospheric responses during two geomagnetic storms on 3 and 4 February 2022. Remote Sens 15(7):1739. https://doi.org/10.3390/rs15071739

Burns AG, Killeen TL, Deng W, Carignan G, Roble RG (1995) Geomagnetic storm effects in the low- to middle-latitude upper thermosphere. J Geophys Res 100(A8):14673–14691. https://doi.org/10.1029/94JA03232

Burton RK, McPherron RL, Russell CT (1975) An empirical relationship between interplanetary conditions and Dst. J Geophys Res 80(31):4204–4214. https://doi.org/10.1029/ja080i031p04204
Cannon P (2013) Extreme space weather: Impacts on engineered systems and infrastructures. Royal Academy of Engineering. https://iswi-secretariat.org/wp-content/uploads/2022/06/Space_Weather_Summary_Report.pdf. Accessed 15 Feb 2002
Community Coordinated Modelling Center (2022) NRLMSISE-00. https://ccmc.gsfc.nasa.gov/models/NRLMSIS~00/. Accessed 15 Feb 2023
Coroniti F, Kennel C (1971) Magnetospheric substorms. In Schindler H (ed). Proceedings of the Conference on Cosmic Plasma Physics, Frascati, September 1971. New York: Springer. 15–23
Crustal Dynamic Data Information System (2022). Total electron content (TEC). https://cddis.nasa.gov/archive/gnss/products/ionex/. Accessed 11 May 2023
Dang T, Li X, Luo B, Li R, Zhang B, Pham K, Ren D, Chen X, Lei J, Wang Y (2022) Unveiling the space weather during the starlink satellites destruction event on 4 february 2022. Space Weather 20(8):1–8. https://doi.org/10.1029/2022SW003152
Davis TN, Sugiura M (1966) Auroral electrojet activity index ae and its universal time variations. J Geophys Res 71(3):785–801. https://doi.org/10.1029/jz071i003p00785
Fang TW, Kubaryk A, Goldstein D, Li Z, Fuller-Rowell T, Millward G, Singer HJ, Steenburgh R, Westerman S, Babcock E (2022) Space weather environment during the spacex starlink satellite loss in february 2022. Space Weather 20(11):1–14. https://doi.org/10.1029/2022SW003193
Fennell JF, Koons HC, Roeder JL, Blake JB (2001) Spacecraft charging: observations and relationship to satellite anomalies. In Harris RA (ed) Spacecraft Charging Technology, Proceedings of the Seventh International Conference, Netherland, April 2001. European Space Agency, ESA SP-476, 279
Gonzalez W, Joselyn J, Kamide Y, Kroehl H, Rostoker G, Tsurutani B, Vasyliunas V (1994) What is geomagnetic storm? J Geophys Res 99(A4):5771–5792. https://doi.org/10.1029/93JA02867
Hardy B P (2020) Long-Term Effects of Satellite Megaconstellations on the Debris Environment in Low Earth Orbit. https://www.ideals.illinois.edu/handle/2142/108004. Accessed 15 Feb 2023
Hastings D, Garrett H (2015) Spacecraft-environment interactions. Cambridge University Press. https://doi.org/10.1017/CBO9780511525032
He J, Astafyeva E, Yue X, Pedatella NM, Lin D, Fuller-Rowell TJ, Fedrizzi M, Codrescu M, Doornbos E, Siemes C, Bruinsma S, Pitout F, Kubaryk A (2023) Comparison of empirical and theoretical models of the thermospheric density enhancement during the 3–4 february 2022 geomagnetic storm. Space Weather 21(9):1–24. https://doi.org/10.1029/2023SW003521
Hoots RF, Roehrich RL (1980) Spacetrack report #3: models for propagation of the NORAD element sets. https://celestrak.org/norad/documentation/spacetrk.pdf. Accessed 20 Feb 2022
Horne RB, Thorne RM, Glauert SA, Albert JM, Meredith NP, Anderson RR (2005) Timescale for radiation belt electron acceleration by whistler mode chorus waves. J Geophys Res Space Physics 110(A3):1–10. https://doi.org/10.1029/2004JA010811
Izurieta EDL, Guamanarca ET, Barbier H (2022) Ionospheric total electron content (TEC) above Ecuador. J Phys Conf Ser 2238:012010. https://doi.org/10.1088/1742-6596/2238/1/012010
Kakoti G, Bagiya MS, Laskar FI, Lin D (2023) Unveiling the combined effects of neutral dynamics and electrodynamic forcing on dayside ionosphere during the 3–4 February 2022 "SpaceX" geomagnetic storms. Sci Rep 13(1):1–15. https://doi.org/10.1038/s41598-023-45900-y
Kamide Y (1992) Is substorm occurrence a necessary condition for a magnetic storm? J Geomagn Geoelectr 44(2):109–117. https://doi.org/10.5636/jgg.44.109
Kamide Y, Perreault PD, Akasofu S-I, Winningham JD (1977) Dependence of substorm occurrence probability on the interplanetary magnetic field and on the size of the auroral oval. J Geophys Res 82(35):5521–5528. https://doi.org/10.1029/ja082i035p05521
Kataoka R, Shiota D, Fujiwara H, Jin H, Tao C, Shinagawa H, Miyoshi Y (2022) Unexpected space weather causing the reentry of 38 starlink satellites in february 2022. J Space Weather Space Clim 12(41):1–10. https://doi.org/10.1051/swsc/2022034
Kennewel J (1999) Satellite orbital decay calculations. IPS Radio and space Service. http://www.ips.gov.au/Category/Educational/SpaceWeather/Space Weather Effects/SatelliteOrbitalDecayCalculations.pdf. Accessed 20 Feb 2022
Klinkrad H (2006) Space debris models and risk analysis. Springer-Verlag, Berlin. https://doi.org/10.1007/3-540-37674-7
Krauss S, Temmer M, Vennerstrom S (2018) Multiple satellite analysis of the earth's thermosphere and interplanetary magnetic field variations due to ICME/CIR events during 2003–2015. J Geophys Res Space Physics 123(10):8884–8894. https://doi.org/10.1029/2018JA025778
Lakhina GS, Alex S, Mukherjee S, Vichare G (2006) On magnetic storms and substorms. In: Gopalswamy N, Bhattacharyya A (eds). Proceedings of the ILWS Workshop, GOA, February 2006, Quest publication. 361–368. https://cdaw.gsfc.nasa.gov/publications/ilws_goa2006/320_Lakhina.pdf. Accessed 20 Feb 2022
Lam MM, Horne RB, Meredith NP, Glauert SA, Moffat-Griffin T, Green JC (2010) Origin of energetic electron precipitation >30 keV into the atmosphere. J Geophys Res Space Physics 115(A4):1–15. https://doi.org/10.1029/2009JA014619
Laskar FI, Eastes RW, Codrescu MV, Evans JS, Burns AG, Wang W, McClintock WE, Aryal S, Cai X (2021) Response of GOLD retrieved thermospheric temperatures to geomagnetic activities of varying magnitudes. Geophys Res Lett 48(15):1–10. https://doi.org/10.1029/2021GL093905
Laskar FI, Sutton EK, Lin D, Greer KR, Aryal S, Cai X, Pedatella NM, Eastes RW, Wang W, Codrescu MV, McClintock WE (2023) Thermospheric temperature and density variability during 3–4 february 2022 minor geomagnetic storm. Space Weather 21(4):1–12. https://doi.org/10.1029/2022SW003349
Li R, Lei J (2021) The Determination of satellite orbital decay from pod data during geomagnetic storms. Space Weather 19(4):1–14. https://doi.org/10.1029/2020sw002664
Lin D, Wang W, Garcia-Sage K, Yue J, Merkin V, McInerney JM, Pham K, Sorathia K (2022) Thermospheric neutral density variation during the "SpaceX" storm: implications from physics-based whole geospace modeling. Space Weather 20(12):1–12. https://doi.org/10.1029/2022SW003254
NASA's Goddard Space Flight Center (NASA GSFC) OMNIweb data documentation. https://omniweb.gsfc.nasa.gov/html/ow_data.html. Accessed 20 Feb 2022
Nikolaeva NS, Yermolaev YI, Lodkina IG (2011) Dependence of geomagnetic activity during magnetic storms on the solar wind parameters for different types of streams. Geomag Aeron 51(1):49–65. https://doi.org/10.1134/S0016793211010099
Nwankwo VUJ, Denig W, Chakrabarti SK, Ajakaiye MP, Fatokun J, Akanni AW, Raulin JP, Correia E, Enoh JE, Anekwe PI (2021) Atmospheric drag effects on modelled low earth orbit (LEO) satellites during the July 2000 Bastille Day event in contrast to an interval of geomagnetically quiet conditions. Ann Geophys 39(3):397–412. https://doi.org/10.5194/angeo-39-397-2021
Oliveira DM, Zesta E (2019) Satellite orbital drag during magnetic storms. Space Weather 17(11):1510–1533. https://doi.org/10.1029/2019SW002287
Patil CG, Rajaram G, Prasad MYS (2008) Correlation of GSO satellite anomalies with space weather data. Acta Astronaut 63(1–4):458–470. https://doi.org/10.1016/j.actaastro.2007.12.050
Picone JM, Hedin AE, Drob DP, Aikin AC (2002) NRLMSISE-00 empirical model of the atmosphere: statistical comparisons and scientific issues. J Geophys Res Space Physics 107(A12):1–16. https://doi.org/10.1029/2002JA009430
Picone JM, Emmert JT, Lean JL (2005) Thermospheric densities derived from spacecraft orbits: accurate processing of two-line element sets. J Geophys Res Space Physics 110(A3):1–19. https://doi.org/10.1029/2004JA010585
Pisacane VL (2008) TThe space environment and its effects on space systems. American Institute of Aeronautics andAstronautics, 1801 Alexander Bell Drive, Suite 500, Reston, VA 20191–4344, USA.https://arc.aiaa.org/doi/book/10.2514/4.862533
Prolss G (2004) Physics of the Earth's space environment (an introduction). Springer Nature, Switzerland. https://doi.org/10.1007/978-3-642-97123-5
Ray V, Berger T, Waldron Z, Sutton E, Lucas G, Knipp D, Thayer J, Hesar S, Scheeres D (2022) The impact of space weather on very low earth orbit (VLEO) satellites. AMOS Tech 2022, 25–30 September 2022. http://amostech.com/2022-technical-papers/. Accessed 7 May 2024
Reiss MA, Möstl C, Bailey RL, Rüdisser HT, Amerstorfer UV, Amerstorfer T, Weiss AJ, Hinterreiter J, Windisch A (2021) Machine learning for predicting the Bz magnetic field component from upstream in situ observations of solar

coronal mass ejections. Space Weather 19(12):1–16. https://doi.org/10.1029/2021SW002859
Ren TL, Liu SQ, Miao J, Luo BX, Wang X, Shi SW (2022) Effects of geomagnetic storms on the accuracy of orbit-derived atmospheric density measurements. Adv Space Res 70(10):2818–2829. https://doi.org/10.1016/j.asr.2022.09.036
Russell CT (2001) Solar wind and interplanetary magnetic field: a tutorial. Geophys Monogr Ser 125:73–89. https://doi.org/10.1029/GM125p0073
Satnews (2022) Starlink satellite loss Explained. https://news.satnews.com/2022/02/13/starlink-satellite-loss-explained/. Accessed 6 Nov 2024
Schwenn R (2006) Space weather: the solar perspective imprint/terms of use. Living Rev Sol Phys. https://doi.org/10.12942/lrsp-2006-2
Shea MA, Smart DF (1998) Space weather: the effects on operations in space. Adv Space Res 22(1):29–38. https://doi.org/10.1016/S0273-1177(97)01097-1
Space (2022) Starlink Decay Report – Februari 2022. https://www.space.com/spacex-starlink-satellites-lost-geomagnetic-storm. Accessed 15 Feb 2022
Space-Track (2022) Two-line element set database. https://www.space-track.org. Accessed 10 Mar 2022
SpaceX (2022) SpaceX report. https://www.spacex.com/updates/. Accessed 16 Feb 2022
Suess ST, Tsurutani BT (2003) Solar winds. Encyclopedia of atmospheric sciences. James R. Holton (ed) Academic Press, Cambridge, Massachusetts, USA. pp 2078–2085. https://doi.org/10.1016/B0-12-227090-8/00373-0
Tapping KF (2013) The 10.7 cm solar radio flux (F10.7). Space Weather 11(7):394–406. https://doi.org/10.1002/swe.20064
Tribble AC (2003) The space environment: Implications for spacecraft design (revised and expanded ed). PrincetonUniversity Press, 41 William Street Princeton, New Jersey 08540, USA. https://doi.org/10.2307/j.ctvzxx9nh
Vallado DA, Crawford P, Hujsak R, Kelso TS (2006) Revisiting spacetrack report #3. AIAA/AAS Astrodynamics Specialist Conference and Exhibits. 2006-6753, 21-24 August 2006. https://doi.org/10.2514/6.2006-6753
Webb DF, Allen JH (2004) Spacecraft and ground anomalies related to the October-November 2003 solar activity. Space Weather. https://doi.org/10.1029/2004sw000075
Word Data Center for Geomagnetism (2022) Transformation of coordinate geographic to geomagnetic (IGRF). https://wdc.kugi.kyoto-u.ac.jp/igrf/gggm/. Accessed 4 Sept 2024
Yuan Z, Liu K, Yu X, Yao F, Huang S, Wang D, Ouyang Z (2018) Precipitation of radiation belt electrons by EMIC waves with conjugated observations of NOAA and van allen satellites. Geophys Res Lett. https://doi.org/10.1029/2018GL080481

Publisher's Note